First results from a borehole network for the seismic characterization of the Einstein Telescope Euregio Meuse-Rhine candidate site

L. D'Onofrio *[1], S. Koley[2], P. Barneo[1], S. Bentvelsen[1], S. Danilishin[5], G. Degrande[3], S. Francois[3], S. Kadmiel[6], M. Kiehn[1], H. Michel[2], F. Nguyen[2], V. Tempel[4], B. Vink[1], W. Walk[1], and others[1]

[1]*Nikhef*
[2]*Universite de Liege*
[3]*KU Leuven*
[4]*RWTH Aachen University*
[5]*Maastricht University*
[6]*KNMI*

Abstract

The low-frequency sensitivity of the Einstein Telescope depends on the seismic environment of its site, both through the mechanical coupling of ground motion to the test masses and through Newtonian noise, which no isolation system can shield. We present the seismic characterization of the Euregio Meuse-Rhine (EMR) candidate site based on a network of recently instrumented boreholes, covering the first seven months of 2026 at four underground stations, together with their co-located surface sensors. Most of these boreholes were deliberately sited next to railway infrastructure, so that the levels reported here describe how anthropogenic noise is generated and attenuated in the local geology. We also introduce `SiteChar`, a general-purpose Python framework developed to make results obtained with different sensors, networks and observation periods directly comparable. It processes the data in sequential chunks and separates the stationary noise floor from the contribution of transients. We present a characterization of the catalog of observed transients and a tentative classification. These measurements form part of an integrated site characterization approach that combines the observed seismic field with three-dimensional geological and wave-propagation models to predict Newtonian noise and ultimately guide its mitigation at the EMR candidate site.

1 Introduction

The extension of Einstein Telescope (ET) sensitivity to frequencies of a few Hertz makes the characterization of the underground seismic environment a central element of site assessment and NN mitigation [1, 2]. At these frequencies, ground motion affects the detector sensitivity both through residual mechanical coupling to the test masses and through gravity fluctuations generated by time-dependent density perturbations in the surrounding medium. The dedicated cryogenic low-frequency interferometer is designed to target approximately the 2–10 Hz band, enabling science including early warning for binary neutron-star mergers, observations of intermediate-mass black holes, and improved tests of gravity in the strong-field regime [3]. This is also the frequency band in which detector performance is most closely coupled to the local environment.

Below roughly 10 Hz [4], the seismic environment enters the sensitivity budget through two distinct mechanisms. The motion of the ground mechanically couples to the test masses through the suspension chain, a contribution that can be suppressed by seismic isolation and by placing the infrastructure underground. However, fluctuations in the local mass density associated with the same ground motion produce a directly coupled gravitational force on the test masses, called Newtonian noise (NN), which

*Corresponding author: `l.donofrio@nikhef.nl`

no isolation system can shield [5]. Site selection and depth can reduce this contribution, while active subtraction using arrays of auxiliary sensors provides an additional mitigation route. Current ET sensitivity projections anticipate the need for NN mitigation in the low-frequency detector, motivating substantial effort toward sensor-array optimisation, next-generation inertial sensors [6–8], and neural-network subtraction methods [9, 10]. The central question for site characterization is therefore not simply how quiet a site is, but whether its seismic environment can be sufficiently characterized and modelled to predict its impact on ET and to design an effective NN mitigation system.

For the same reason, the comparison between candidate sites (the Sos Enattos area in Sardinia (Italy); the Euregio Meuse-Rhine (EMR) at the border between the Netherlands, Belgium and Germany; and the Lusatia site in Saxony (Germany)) cannot be reduced to a comparison of ambient noise amplitudes. The conversion from ground motion to gravity fluctuations depends on the composition of the seismic wavefield, on its spatial coherence, and on the local geology, so that sites with comparable displacement spectra may differ appreciably in their NN projections, and viceversa. The relevant quantities are thus the wave content and coherence length of the field, its stability in time, the occurrence and characteristics of anthropogenic transients, and the extent to which all of these can be measured by an auxiliary array and used for subtraction.

In the EMR programme, this motivates an explicitly integrated approach to site characterization. Rather than treating geology, seismic observations, and NN modelling as separate activities, the EMR strategy is to combine the measured seismic field with a detailed three-dimensional geological model and physics-based simulations of seismic wave propagation. The resulting displacement field can then be translated into gravitational perturbations at the detector test masses, including the influence of the underground infrastructure, and used to develop and optimise mitigation strategies. A distinctive feature of the EMR site characterization programme is therefore the development of this integrated, site-specific modelling chain, connecting geological structure, measured seismic fields, wave propagation, NN prediction, and mitigation. This approach is designed to move beyond the characterization of individual site properties towards a physics-based prediction of how the complete underground environment affects ET performance.

Previous underground campaigns in the EMR area have shown that the seismic field is dominated by a nearly continuous stochastic background of body waves with random incidence angles, rather than by surface waves [11, 12]. Under the assumptions adopted in those studies, the resulting NN estimate lies above the ET-D design sensitivity by up to about a factor of two below ~ 8 Hz, with the largest margin required in the 3–6 Hz band; the same analyses indicate that increasing the depth beyond ~ 250 m would bring limited additional benefit, since the body-wave background is only weakly depth-dependent. These estimates depend on assumptions concerning the composition and spatial properties of the seismic field. The new borehole network provides substantially longer and more spatially distributed observations with which these assumptions can be tested and the site-specific models refined.

A further aspect of the seismic environment concerns its non-stationary component. Anthropogenic activity in the surrounding area produces transient disturbances that are superimposed on the ambient background, and whose contribution is not captured by long-term averaged spectra. Their characterization, in terms of spectral signature, occurrence statistics and spatial extent, is therefore a natural complement to the description of the stationary field and provides part of the input needed for a realistic description of the environment in which the detector would operate.

In this work, we characterize the seismic environment of the EMR candidate site using the first seven months of data from the recently deployed borehole network. We separately quantify the stationary seismic background and the non-stationary transient population, with particular emphasis on railway-generated disturbances and their attenuation between surface and underground stations. Because most of the boreholes considered here were intentionally located close to railway infrastructure, these measurements should not be interpreted as representative noise levels at prospective detector vertices but they provide controlled observations of anthropogenic source generation, propagation and attenuation through the local geology. The resulting measurements provide constraints for the three-dimensional wave-propagation and NN models being developed for the EMR site.

To ensure consistent analysis across stations, sensors and observation periods, we developed the Python-based `SiteChar` framework and used throughout this work. It provides a common processing pipeline and allows to separate the stationary background from transient contributions.

The paper is organized as follows. Section 2 describes the site, the instrumentation, the dataset and the strategy toward full coherent understanding of the noise. Section 3 introduces the `SiteChar` package and the spectral estimators it defines. Section 4 presents the background noise characterization, while Section 5 focuses on the transient population and on the coincident detection. Section 6 summarizes the results and outlines future work.

2 The EMR candidate area and station layout

The EMR candidate area lies at the border between the Netherlands, Belgium and Germany. The shallow subsurface is characterized by a soft sedimentary cover of variable thickness overlying a hard Palaeozoic bedrock, with a pronounced impedance contrast at the interface [12]; the depth and nature of this transition differ appreciably from one location to another, and this heterogeneity is itself one of the quantities the ongoing campaign is designed to constrain.

Long-term reference observations in the area are provided by the underground station at Terziet (TERZ), operating at 250 m depth. As part of the ongoing exploration effort, a set of recently drilled boreholes has been instrumented with broadband seismometers at the surface and borehole, at Obsinnich (OBSN), Teuven (TEUV), and Beusdael (BSDL); further boreholes at Hoof, Asse, Herbesthal are being completed and instrumented, and are not covered by the present analysis.

It should be emphasised, and it is essential for the interpretation of all the results presented below, that most of these boreholes were *deliberately* positioned in unfavourable locations (see Figure 1). Of the stations considered here, only BSDL is close to an envisaged corner point of the detector. OBSN and TEUV were chosen specifically to study the generation, propagation and attenuation of anthropogenic noise in the local geology, and therefore do not represent the noise conditions expected at candidate corner-point positions. The relevant characteristics are:

- **Obsinnich (OBSN)** is located about 60 m from an active railway line and railway bridge, with train traffic throughout the day and night. The borehole sensor is installed at 280 m. Additional structures in the vicinity include the Viaduct of Remersdaal, roughly 530 m to the east, whose pillars are founded in the bedrock, and a tunnel portal about 940 m to the west.
- **Teuven (TEUV)** lies approximately 200 m from a railway tunnel, again with traffic distributed over the whole day, with the borehole sensor at 260 m.
- **Beusdael (BSDL)** is the only station of this set close to a possible corner-point location. It is instrumented at three levels: at the surface, at 30 m and at 320 m. The station was installed on 11 February 2026 but the sensors experienced different problematics. In this work, we consider only the underground sensor at 320 m for a specific time window.

The surface sensors are Güralp 3ESPC three-component broadband seismometers, while the borehole sensors, at both intermediate and total depth, are Nanometrics Trillium Compact Post-Hole 120 s three-component broadband seismometers. At Terziet, a malfunctioning Kinemetrics STS-5 was replaced by a Trillium Compact Post-Hole unit, which has been recording since 11 November 2025; the power spectral densities obtained with the two configurations are in agreement, so that the continuity of the reference dataset is preserved. Data are recorded continuously at a sampling rate of 40 Hz; all spectra shown in this work are corrected for the instrument response and expressed in acceleration units but converted in dB with no explicit normalization constant, which corresponds to an implicit reference of 1 $(m/s^2)^2$/Hz. For example: PSD $= -140$ dB re 1 $(\mathrm{m/s^2})^2/\mathrm{Hz}$ converts back to linear units as $10^{-140/10} = 10^{-14}(\mathrm{m/s^2})^2/\mathrm{Hz}$ The analysis strategy adopted throughout this work and the definitions of the spectral quantities used are described in the next section.

Figure 1: Map of the EMR candidate area around the Terziet area showing the installed stations and the main transport infrastructure in their vicinity (credits to Google Maps).

3 The `SiteChar` package: a general-purpose framework for site characterization

Characterizing the seismic environment of a candidate site is a necessary step in site selection and monitoring towards the ET site selection. In practice, this work is often repeated independently for each site, using ad-hoc scripts tailored to the specific sensors, and network conventions in use at that location. This duplication of effort makes results difficult to compare across sites and slows down the iterative process of site evaluation. `SiteChar` was developed to address this: a single, general-purpose analysis framework that separates the *scientific question* being asked (how noisy is this site, how often do transients occur, how do they propagate between sensors) from the *specifics of any one deployment* (sensor type, data format, network convention, deployment duration).

`SiteChar` is deliberately agnostic to the physical nature of the sensor and to the geographic scale of the deployment. The same analysis can be applied uniformly to a single borehole seismometer, to a pair of co-located surface and borehole sensors at one station, or to a set of geographically distant stations belonging to entirely different monitoring networks. This generality is achieved by defining the framework around a minimal set of physical concepts (a *sensor*, a *station* grouping co-located sensors, and a *network* grouping distinct stations for comparison). Adding a new site, or a new class of sensor beyond seismometers (e.g. magnetometers, microbarometers), requires only implementing the data-loading step for that source.

For long-term characterization, `SiteChar` processes the data in sequential chunks (typically two hours), retaining only the derived spectral products needed for characterization and discarding the raw samples once each chunk has been processed. This makes multi-month characterization runs practical on standard hardware.

Transients (e.g. passing trains, vehicle traffic, or other anthropogenic disturbances) are identified from the time-frequency structure of the signal. For each analysis window, a spectrogram is computed and, at each frequency, the power is converted to a robust z-score relative to the median and median absolute deviation across time (see details in Section 3.1). A time sample is flagged as part of a transient if its z-score, integrated over a chosen frequency band of interest, exceeds a specific threshold for a minimum duration; adjacent flagged samples are merged into a single detected event.

For every analysis chunk, `SiteChar` defines three different spectral quantities:

- The **chunk spectrum** is the power spectral density computed over the entire analysis chunk (typically two hours), with no exclusion of transients. It answers the question "what does the ambient seismic field look like overall, transients included, averaged over this period?".

- The **background spectrum** is computed only over the longest transient-free interval identified within the same chunk, using the transient detection to exclude all flagged intervals (with a guard margin around each). It answers a different question: “what is the seismic field like in the absence of the fast disturbances that were detected?”.

- The **event spectrum** is computed over an individual detected transient, and is always paired with the background spectrum of the same chunk to form an event-to-background ratio. This ratio quantifies how much a given transient elevates the noise level above the ambient background, as a function of frequency.

Because `SiteChar` core analysis is independent of sensor type and network, the results obtained at one candidate site are directly comparable to the results obtained at any other, without requiring each site to be re-implemented as a separate analysis pipeline. This is particularly valuable in the context of a multi-sensors (or multi-site) characterization campaign: candidate locations are typically instrumented by different groups, using different sensor models and different data archives, over different observation periods, yet the resulting background levels and the transient statistics need to be placed on a common footing to support an objective site comparison. `SiteChar` is intended to serve as the common analysis layer.

3.1 Z-score

Transients are identified independently on each sensor from a normalized spectrogram statistic. The record is processed in consecutive blocks of two hours, each loaded with 600 s of padding on either side so that the transients of the response deconvolution fall outside the analyzed interval, and transformed with a Hann-tapered short-time Fourier transform using 20 s segments and 50% overlap, giving $\Delta t =$ 10 s and $\Delta f = 0.05$ Hz. Writing $S(f,t)$ for the resulting power spectral density, each frequency row is standardised by its own median $m(f) = \mathrm{med}_t \log_{10} S(f,t)$ and median absolute deviation $\mathrm{MAD}(f) = \mathrm{med}_t \,|\log_{10} S(f,t) - m(f)|$, both evaluated over all columns of the block.
The detection statistic is the median of the standardized spectrogram across the analysis band $[f_1, f_2] =$ $[2, 15]$ Hz:

$$z(t) = \underset{f_1 \le f \le f_2}{\mathrm{med}} \frac{\log_{10} S(f,t) - m(f)}{\mathrm{MAD}(f)}. \tag{1}$$

Columns with $z(t) > z_{\mathrm{thr}} = 2.5$ are flagged and contiguous flagged columns are merged into triggers. Since $\log_{10} S$ is a logarithmic power, the statistic converts to physical units through a single factor: one unit of z corresponds to $10\,\overline{\mathrm{MAD}}$ dB above the local background, where $\overline{\mathrm{MAD}}$ is the band median of $\mathrm{MAD}(f)$, equal to generally 3.5 dB on these channels, so that z_{thr} represents an excess of about 8–9 dB. **VERIFY**

The construction assumes that the ambient noise is stationary within a block, that transients occupy a minority of it so that the median and the median absolute deviation still describe the stationary state, and that the signals of interest are broadband, since the median in Eq. (1) responds only when more than half of the frequency bins rise together. The median absolute deviation is used unscaled, so z_{thr} is an empirical operating point and not a Gaussian tail probability. The main advantage of this design is that no external calibration is required.

Because the normalisation is re-estimated on every block, a fixed threshold in z does not correspond to a fixed physical amplitude: the absolute level required to trigger follows the diurnal cycle of the ambient noise, varying by approximately 10 dB between night and midday (Fig. 2), so the catalog is not amplitude-complete in an absolute sense and weaker transients are recovered at night but missed during the day.

3.1.1 Duration of a trigger

A trigger is a contiguous set of spectrogram columns with $z(t) > z_{\mathrm{thr}}$, but its extent depends on the signal amplitude and therefore does not directly measure the transient duration.

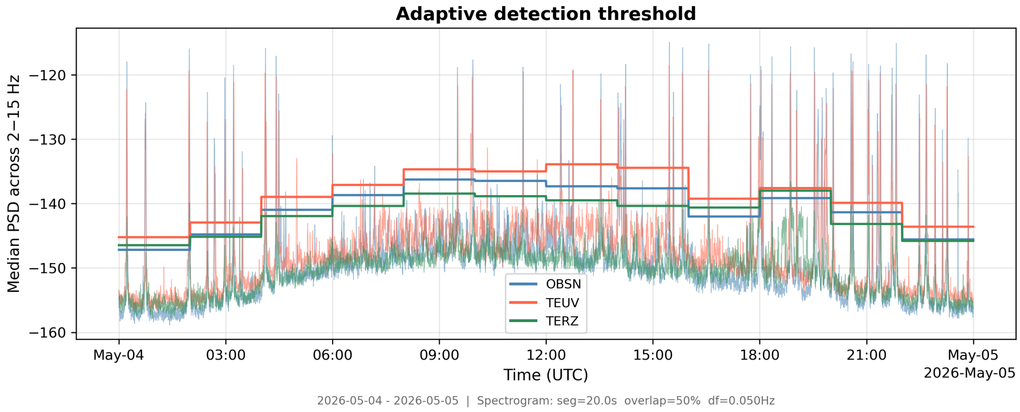

Figure 2: Detection threshold in physical units for the analysis of one day (4 May 2026). Thin lines: median power spectral density across the 2–15 Hz band, one value per 10 s spectrogram column, for the three underground vertical channels. Thick lines: the corresponding detection threshold, obtained by re-estimating the per-frequency median and median absolute deviation on each 2 h block and applying the fixed z-score threshold z = 2.5 used throughout this work. The vertical distance between the two lines of a given colour is the detection statistic itself, at 3.9 dB per unit z. Because the normalisation is re-estimated locally, a fixed z corresponds to an absolute level that follows the diurnal cycle of the ambient noise, spanning about 10 dB between night and midday.

We therefore use the equivalent duration of the band envelope. The instrument-corrected acceleration is band-passed to 2–15 Hz with a fourth-order Butterworth filter. The nstantaneous power envelope $E(t)$ is obtained from the Hilbert transform, smoothed over 1 s, and corrected for the local baseline E_0. Defining

$$\tilde{E}(t) = \max\left[E(t) - E_0,\, 0\right], \tag{2}$$

the equivalent duration is

$$T_{\mathrm{eq}} = \frac{\left[\int \tilde{E}(t)\,\mathrm{d}t\right]^2}{\int \tilde{E}^2(t)\,\mathrm{d}t}, \tag{3}$$

evaluated over a window of half-width $\max(3\,\tau_{\mathrm{trig}}, 150\,\mathrm{s})$ centred on the trigger where τ_{trig} is the trigger duration. This measure is independent of amplitude for a fixed envelope shape and is not limited by the spectrogram cadence. The equivalent duration T_{eq} can be defined as the duration of a rectangular pulse with the same energy and effective power as the observed transient (see Figure 3).

Because the search window has a minimum half-width of 150 s, neighbouring triggers may contaminate the event window. We therefore record the distance to the nearest trigger at the same station and flag events as isolated when no neighbour falls inside the window.

4 Background seismic noise characterization

The analysis covers the period from 1 January 2026 to 1 August 2026, processed in sequential two-hour chunks as described in Section 3. For each chunk, both the chunk spectrum and the background spectrum are computed, so that the stationary noise floor can be separated from the contribution of the detected transients.

The BSDL station became operational only on 11 February 2026, and none of its borehole channels covers the full January–August window. The deepest instrument at 320 m depth, was initially affected by problems that occurred during its installation, which compromised the coupling of the sensor to the borehole casing.

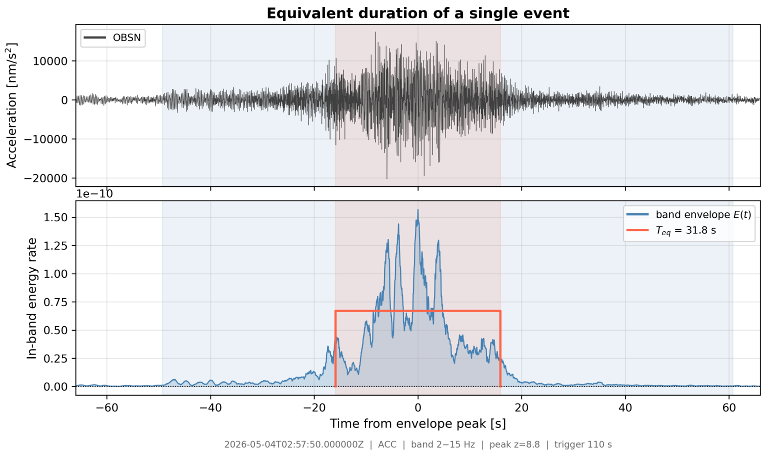

Figure 3: Equivalent duration of a single event at station OBSN. Top: ground acceleration. Bottom: in-band energy rate $E(t)$, the squared analytic envelope of the 2–15 Hz signal smoothed over 1 s, with the boxcar of equal area, of width $T_{\rm eq} = (\int E)^2/\int E^2$ and height $\int E^2/\int E$, centred on the envelope peak. The blue band marks the trigger returned by the detector, the red band the $T_{\rm eq}$ integration window.

Throughout this work only the vertical component is analyzed. The azimuthal orientation of the borehole horizontal components is not independently constrained, so the horizontal traces cannot yet be rotated into a common reference frame for a station-to-station comparison. Orientations can in principle be recovered from the polarisation of earthquakes, and this is left to a forthcoming study. The horizontal components carry information that is essential for NN estimation and cannot be neglected in the long term.

4.1 Background analysis

The background spectra discussed in this section are computed on the longest transient-free interval of each two-hour chunk, as defined in Section 3. The number of chunks effectively available differs from station to station (Figure 4). The missing coverage is not uniformly distributed in time: TERZ has a gap in January–February, while BSDL is available only from March, so that the four datasets sample different fractions of the seasonal cycle and no period exists in which all sensors were simultaneously operational.

Figure 4 shows the time evolution of the background PSD over the analysis period, with a resolution of two hours since each row is the background spectrum of one chunk. The microseismic band exhibits the expected seasonal decay, with levels progressively decreasing from January–March towards May–June by ~ 10 dB, in agreement with the North Atlantic wave forcing (Appendix A). A diurnal modulation of the noise floor is visible at all stations above 1 Hz; its amplitude is quantified in Figure 10 and amounts to 5–8 dB in the 2–15 Hz band power between the nighttime minimum and the midday maximum. This modulation of the background, and not of the sources, is what makes the detection statistic of Section 3.1 intrinsically relative and is used in Section 5.3 to interpret the hourly distribution of the detections.

Two families of features stand out from the diffuse background. Horizontal stripes, short-lived and broadband in the microseism band, correspond to teleseismic events; their identification and their signature in the detection statistic are discussed in Appendix B. Vertical stripes, narrow in frequency and persistent over the whole observation period, correspond to spectral lines: the most prominent one is the line at ~ 3.125 Hz, clearly visible at OBSN and TEUV and weaker at TERZ and BSDL, which also appears as a sharp spike in the median spectra of Figure 5 and as a continuous horizontal feature in the stacked spectrograms of Figure 6. The amplitude of these lines is not stationary and their origin has not yet been established; candidate explanations include nearby rotating machinery,

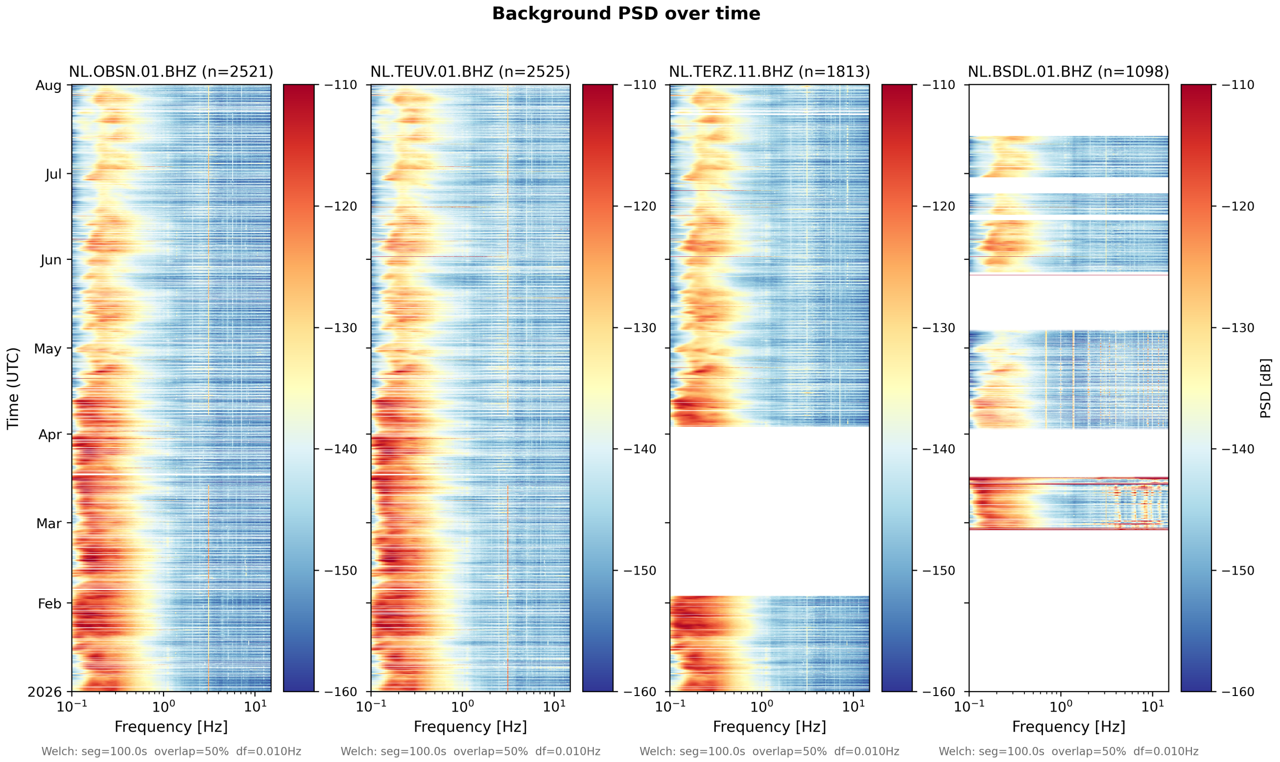

Figure 4: Time evolution of the background PSD at each borehole station over the January–August 2026 analysis window. Each column corresponds to one station; the vertical axis is calendar time (UTC), the horizontal axis is frequency on a logarithmic scale. Colour encodes PSD level in dB. White regions indicate gaps in data coverage. Seasonal and diurnal variations in the noise floor are visible in all the stations.

pumping or ventilation equipment.

The BSDL borehole sensor requires a separate remark. The channel is available from March, but the first weeks are dominated by the residual disturbances of the installation, visible in Figure 4 as an unstable and elevated noise floor, and are therefore not representative of the site. Only the chunks after 15 May 2026 are used in the following.

Figure 5 (top panel) shows the median background PSD and the 5^{th}–95^{th} percentile range for the four borehole sensors. Below ~ 0.5 Hz the spectra of all stations are dominated by the secondary microseismic peak at ~ 0.2 Hz, with median levels between -124 and -117 dB. The apparent spread of a few dB between stations is not a property of the sites but a consequence of the different temporal coverage discussed above, since the microseismic amplitude is modulated by the seasonal cycle of ocean-wave activity. When the comparison is restricted to the time slots common to all stations the peaks coincide to within a fraction of a dB (Figure 15). Between ~ 0.5 and ~ 1 Hz all sensors converge towards a common minimum of about -148 dB, and above 1 Hz they remain within a few dB of one another, TERZ defining the lowest floor at about -150 dB.

The main result of this comparison is therefore the similarity of the four curves. Once the fast non-stationarities are excluded, four boreholes drilled in different geological conditions, at depths between 250 and 320 m, and at distances from the railway ranging from tens of metres to several kilometres, describe essentially the same stationary field. It should be stressed that the exclusion concerns only the fast non-stationarities: the slow ones survive in these spectra, since each curve is a median over chunks that span the diurnal cycle, the weekly cycle and the seasonal modulation of the microseism, all of which contribute to the width of the percentile bands.

The chunk spectra of the bottom panel behave in the opposite way since the stations separate clearly above 1 Hz, and the ordering follows the distance from the railway line. OBSN and TEUV,

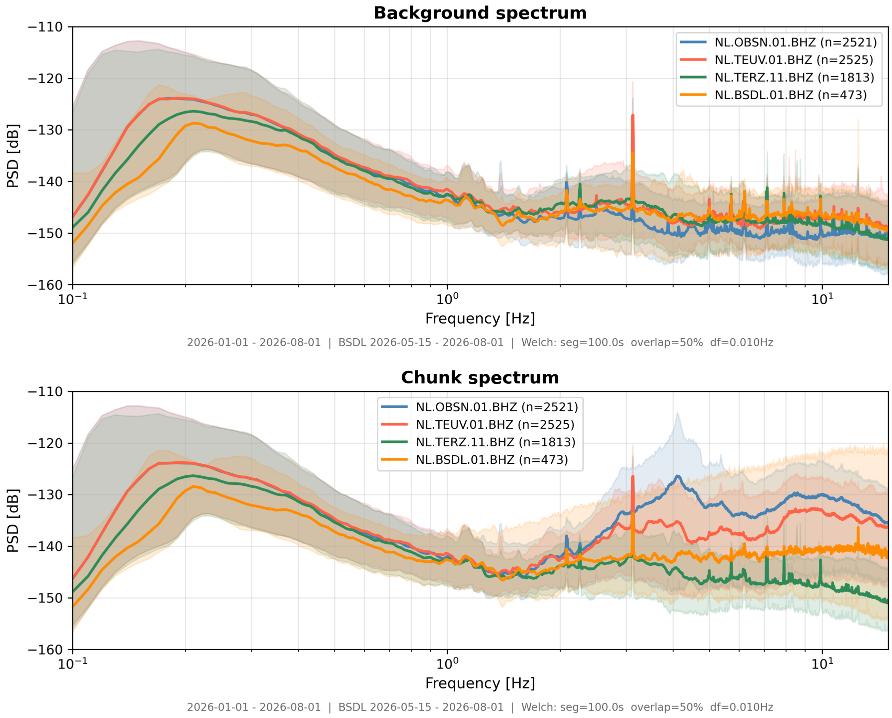

Figure 5: PSD comparison across the four underground borehole stations (OBSN, TEUV, TERZ, BSDL) over the January–August 2026 analysis window. Solid lines show the median, shaded bands the 5^{th}–95^{th} percentile range. Left: background noise estimated from the longest quiet stretch in each 2-hour chunk. Right: full-chunk PSD including train passages. The difference between the two panels reflects the spectral contamination introduced by transient sources, predominantly above 1 Hz. For BSDL, we considered only the data after the 15 of May.

the two stations sited next to the infrastructure, lie well above TERZ, which is the farthest from it. The hierarchy is thus a property of the transient population and of its duty cycle, not of the sites themselves. The pair of estimators defined in Section 3 keeps the two contributions separate: the background spectrum measures what the site is, while the difference between the two panels measures how often, and by how much, it is perturbed.

5 Transient event characterization at EMR

In this section we describe the characterization of the transient catalog detected in the first seven months of 2026. Transients are identified with the time-frequency z-score statistic defined in Section 3.1, evaluated in the 2–15 Hz band with a threshold $z_{\text{thresh}} = 2.5$ and a minimum duration of 10 s. Section 5.1 analyzes one passage in detail coincident at the four underground sensors, using the co-located surface sensors. Section 5.3 describes the catalog as a whole while Section 5.4 uses the coincidence between stations to separate the populations that compose it.

5.1 Analysis of a single transient

The single-event analysis is presented for a passage detected at the four borehole stations on 2026-07-12 around 02:48 UTC. The event is one entry of the catalog, and the window analyzed is the two-hour chunk it comes from. For the single-event analysis we consider also the surface sensor of each station, for which a similar trigger detection with the same parameters has been performed.

Two windows are used throughout. The *event window* is T_{eq}–wide and centred on the maximum of the 2–15 Hz energy envelope, which is the same window on which the detection measures T_{eq} defined

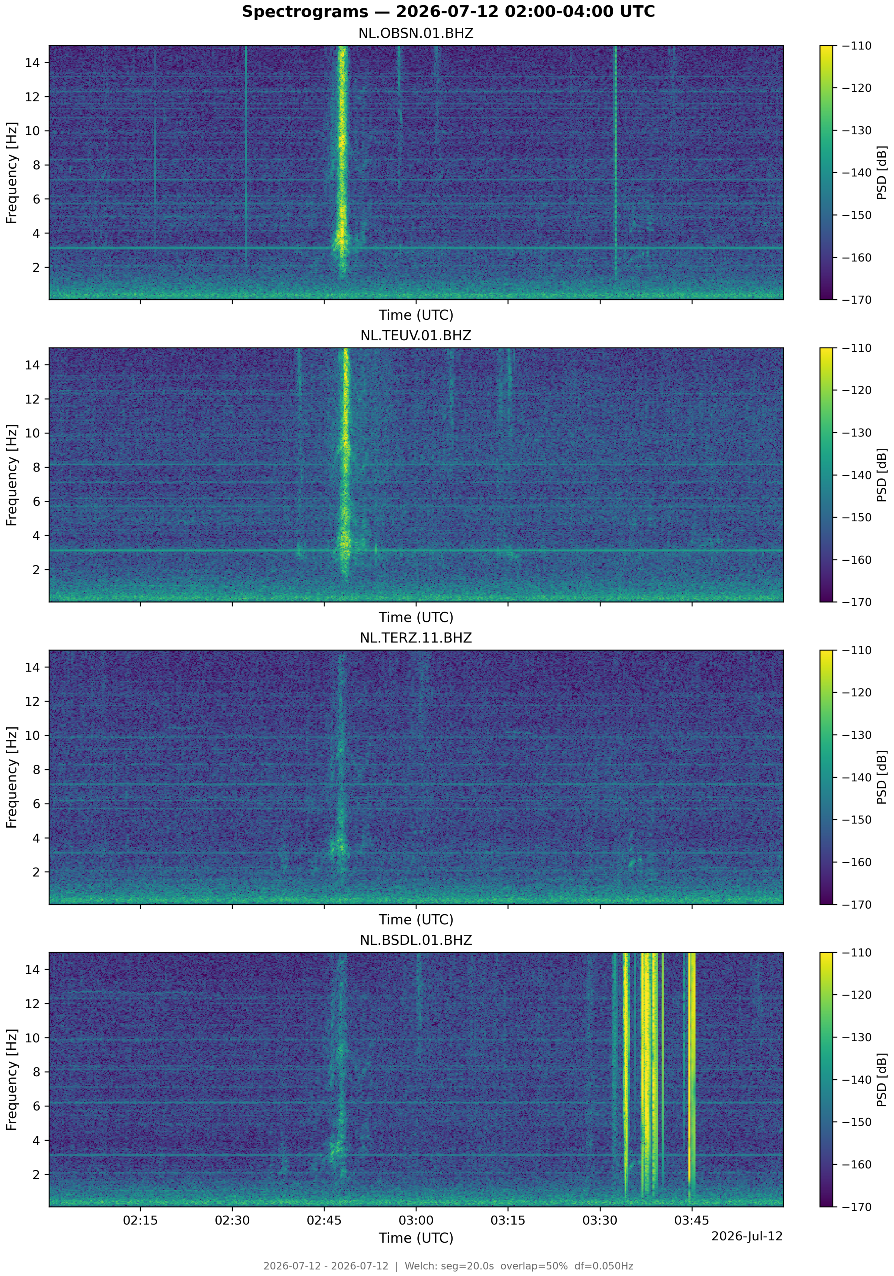

Figure 6: Stacked spectrograms of the two-hour analysis chunk (02:00–04:00 UTC, 2026-07-12) at the four borehole sensors. The passage analyzed in Section 5.1 appears as the broadband vertical burst near 02:48 UTC, visible at all four stations with station-dependent amplitude. The continuous horizontal line at ~ 3.1 Hz is the spectral line discussed in Section 4, unrelated to the passage.

per station. The *background window* is the longest contiguous stretch of the chunk in which *neither* sensor of the station has a trigger, with a guard of 60 s around each. The requirement on both sensors is essential: the surface detects considerably more events than the borehole, so a stretch that is quiet for the borehole is not necessarily quiet at the surface, and a contaminated reference inflates the measured attenuation.

The surface sensor is counted as having recorded the event if its z exceeds the detection threshold inside the T_{eq} window of the borehole. Where the surface does not cross the threshold the event is not measurable, but it is bounded from above, since its surface PSD is at most the surface background; the attenuation panel then shows that bound as a dashed line in place of the event curve. This case is not rare and is itself a result: at TERZ and BSDL the passage remains above the borehole noise

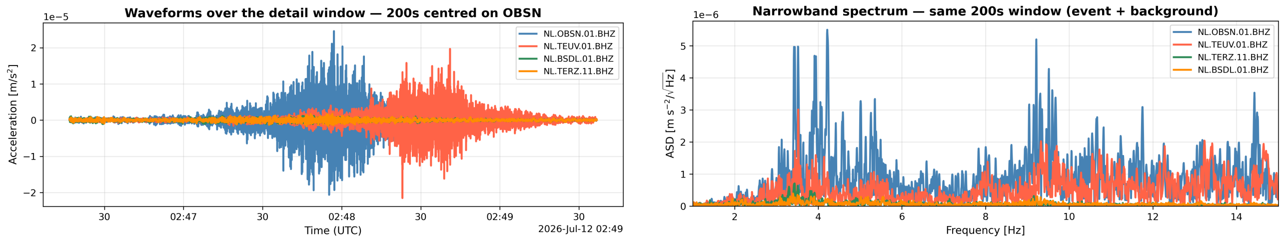

Figure 7: The passage shown in Figure 6 seen on a single 200 s window common to the four stations, centred on the envelope peak at OBSN. *Left:* (a) instrument-corrected acceleration, drawn in order of decreasing z. *Right:* (b) amplitude spectral density on the same window, obtained from a single Hann-tapered FFT with no averaging, so that $\Delta f = 1/T$. This panel is intended to resolve spectral lines and not to read noise levels.

floor while falling below the surface one, which is 20–30 dB higher, so that the gain in detectability provided by the depth can be quantified event by event.

Figure 6 shows the two-hour data at the four borehole sensors. The transient appears as a broad-band vertical burst, almost simultaneous within the resolution of the spectrogram and with station-dependent amplitude. The corresponding detection statistic is shown in Figure 18 for the borehole and for the surface sensors, together with the background window actually used. Figure 7 shows the waveforms of the four stations on a common 200 s window and the narrowband spectrum computed on the same window with a single Hann-tapered FFT to resolve spectral lines. The narrowband spectrum shows structured lines around 4, 5 and 9 Hz and it can be considered the spectral signature of the event.

Figure 8 shows the event-to-background ratio at the four stations. The ratio is compatible with 0 dB below 1 Hz and rises steeply above it, reaching 30–50 dB in the 3–15 Hz band, with the largest excess at OBSN, the station closest to the track. The shape of the ratio is remarkably similar at the two stations close to the line, OBSN and TEUV, which differ mainly by an overall offset, whereas TERZ and BSDL depart from it around 10 Hz, where their excess flattens or decreases instead of continuing to rise. This is consistent with the high-frequency content of the transient being attenuated over the propagation distance.

The comparison with the co-located surface sensors is presented in Figure 9. In the absence of transients, the surface and the borehole sensor of the same station are almost fully coherent below ~ 0.5 Hz, where both are driven by the microseismic field. The background coherence collapses above ~ 1 Hz: the ambient high-frequency fields at the surface and at depth are essentially independent. During the event the coherence remains significant, although strongly structured, up to 10 Hz at the stations where the surface crosses the threshold. The two curves average a very different number of segments, a few units for the event against hundreds for the background, and therefore have different statistical floors (dashed lines). The surface-to-borehole attenuation grows from ~ 0 dB below 0.3 Hz to 40–50 dB above 5 Hz, and is reported at different resolutions for the two windows.

It should be noted that the surface background is not stationary, and both the coherence and the attenuation estimated on the event window can be affected by this. At OBSN, the event coherence between surface and borehole decreases below 1 Hz while the background remains fully coherent, and the event attenuation rises at low frequency where the background attenuation is flat at 0 dB; TEUV, 200 m from the line, shows nothing of the sort for windows of the same length. The same behaviour is observed for other transients at OBSN, which points to an effect related to the proximity of the railway line.

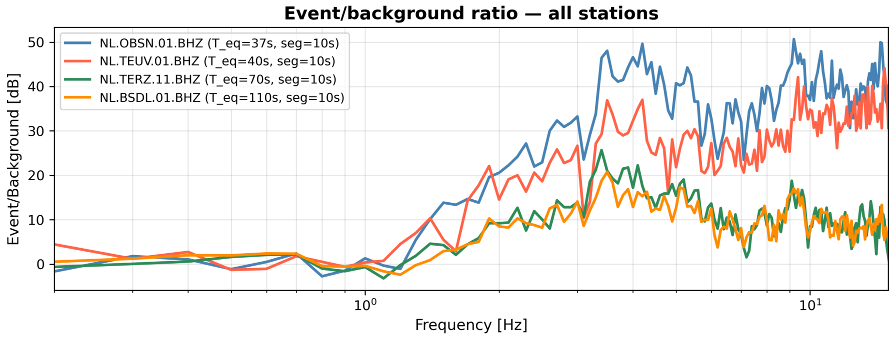

Figure 8: Event-to-background PSD ratio for the passage of Figure 6, at the four borehole sensors. For each station the ratio is computed between the PSD of its own T_{eq} window, centred on the local envelope peak, and the PSD of the background window of the same chunk. The equivalent duration and the Welch segment used are reported in the legend; the growth of T_{eq} from OBSN to BSDL follows the decrease of the signal-to-noise ratio and is discussed in Section 5.1.

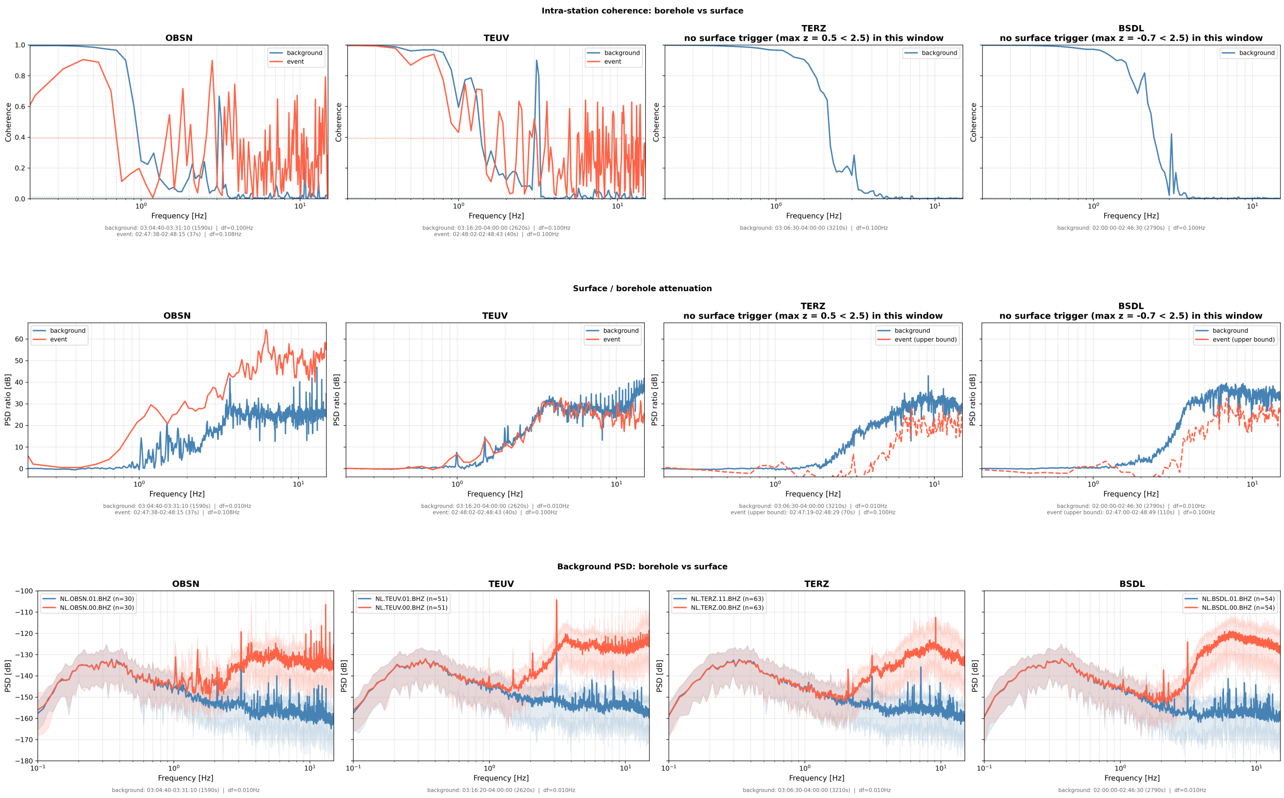

Figure 9: Each column corresponds to one station and, in every panel, blue refers to the background window and red to the event window. *First row:* () surface-to-borehole coherence. The two curves average a very different number of segments and each must be read against its own 95% significance level (dashed lines). *Second row:* () surface-to-borehole PSD ratio, i.e. the attenuation provided by the combination of the soft cover and the depth. Where the surface sensor does not cross the detection threshold inside the T_{eq} window, the event curve is replaced by the dashed upper limit given by the surface background. *Third row:* () background PSD of the surface and borehole sensors separately, with the shaded bands giving the 5^{th}–95^{th} percentile range. Welch parameters and the number of averaged segments are reported under each panel.

5.2 Modelling

5.3 The 2026 event catalog

Over the analysis period the detection rate, normalized to the hours actually analyzed, is 3.5 and 2.9 events per hour at OBSN and TEUV, 0.7 at TERZ and 2.6 at BSDL, corresponding to 17 488 and 14 627 triggers over 5042 and 5050 analyzed hours at the first two stations, 2594 over 3626 hours at TERZ and 2493 over 946 hours at BSDL, the latter restricted to the data after 15 May 2026 as in Section 4. Combined with the median durations reported below, the flagged samples represent $\sim 3.5\%$ of the analyzed time at OBSN and TEUV, $\sim 1.4\%$ at TERZ and $\sim 0.4\%$ at BSDL. At this stage the rates are not directly comparable between stations, because the catalogs do not contain the same mixture of populations: the median equivalent duration is 5.4 s at BSDL against 38–70 s at the other three stations, and OBSN too carries a substantial number of short-duration triggers. These are of a different nature from the railway transients and are discussed separately in Section 5.5.

Panel (a) of Figure 10 shows the distribution of the equivalent durations T_{eq} defined in Section 3.1. At OBSN, TEUV and TERZ the distributions are unimodal and positively skewed, with medians of 37.6, 43.6 and 70.0 s respectively. BSDL is qualitatively different, its distribution piling up at the shortest durations with a median of 5.4 s, for the reason discussed above. The larger median at TERZ should be read together with the behaviour of the estimator described in Section 5.1: TERZ is the station with the lowest signal-to-noise ratio, and part of the shift is a property of T_{eq} at low SNR rather than of the sources.

Panel (b) shows the in-band energy of each event as a function of the duration. The energy measures the total disturbance deposited at the site: a long weak transient and a short loud one can perturb it by the same amount. No clear trend with duration is present at any station but the plane shows that the catalog is not a single population. At OBSN the events separate into two branches about 12 dB apart in energy, with a gap between them that a threshold effect alone would not produce, and a similar although less pronounced structure is visible at TEUV. This separation in energy is the starting point of the classification of Section 5.4.

Panel (c) shows the hourly distribution of the detections. OBSN and TEUV, the two stations closest to the railway, show an almost flat pattern. TERZ shows a marked pattern with maxima in the early morning and late evening and a pronounced minimum during working hours, while BSDL shows the opposite behaviour, with more, and more energetic, events during the day.

These three patterns have different origins and it is important not to read them all as a modulation of the source activity. Panel (d) shows the absolute band power of the detected events, measured over their T_{eq} window, together with that of the background windows, on the same scale. The event level is essentially independent of the hour of the day, whereas the background follows a clear diurnal cycle of 5–7 dB, with the minimum around 02–04 UTC and the maximum around 10–12 UTC, at all four stations. Since the detection threshold is defined relative to that background, the same physical disturbance is more easily detected at night, and the nocturnal excess of detections at TERZ is largely a selection effect of the relative threshold. The flat pattern of OBSN and TEUV, where events exceed the local floor by tens of dB, is instead robust against this bias.

Panel (e) shows the detection rate as a function of the day of the week, normalized to the hours actually analyzed for each weekday, so that the uneven coverage of the four stations does not enter the comparison. A population dominated by the freight train traffic is expected to show a moderate reduction at the weekend.

The panels of Figure 10 describe the catalog as a single population and show that it is not one. However, assigning each event to a source is not possible with the present data: no reliable database of the railway traffic, with the characteristics of the individual convoys, is available for the period, and none of the observables shown here is by itself decisive on a single event. What can be done, and is the subject of the following Section, is to use the coincidence between stations as a statistical ordering criterion, and to describe the populations that emerge from it.

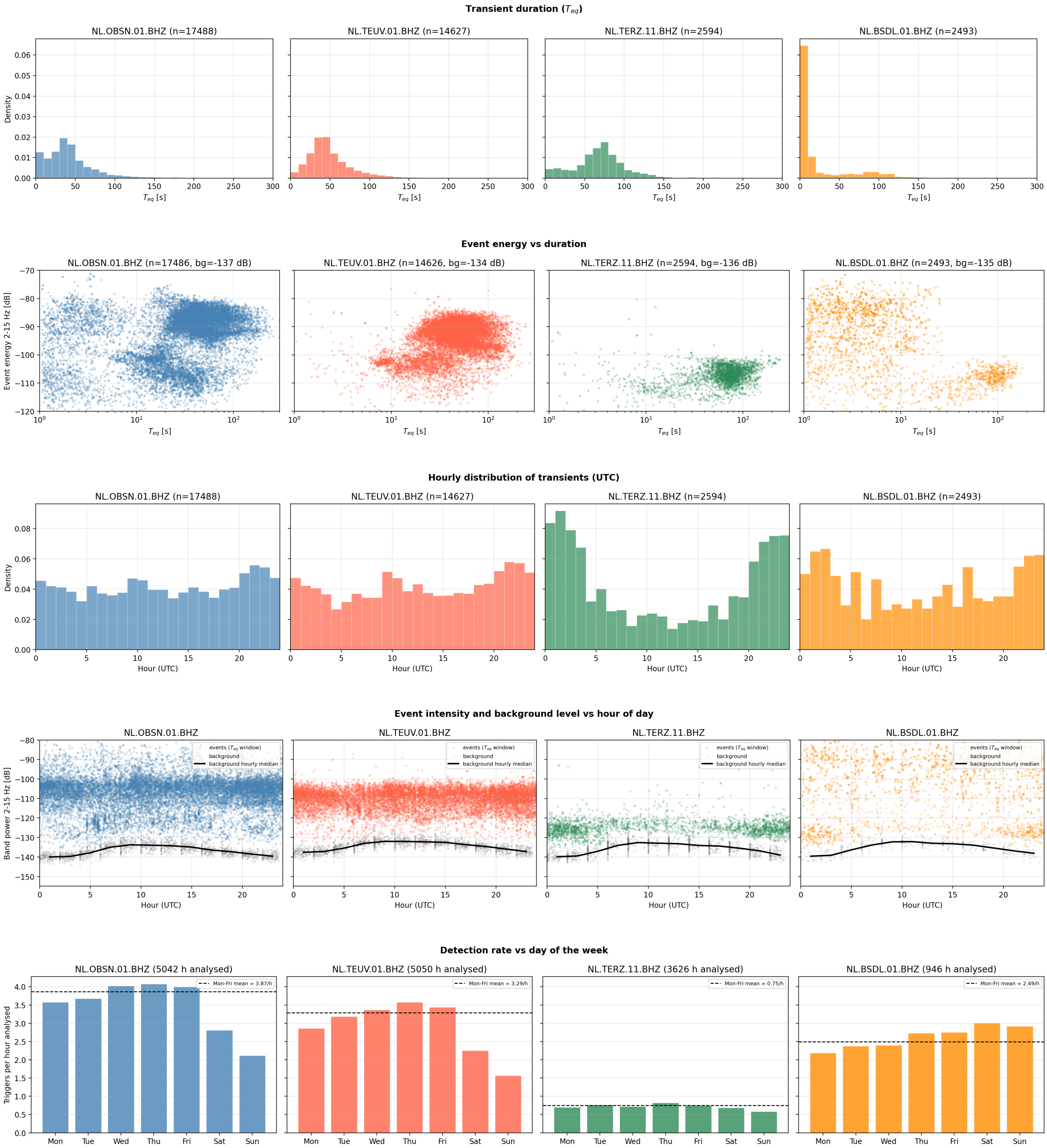

Figure 10: Statistical characterization of the transients detected at the four stations over the first seven months of 2026, with BSDL restricted to the data after 15 May. *First row:* distribution of the equivalent duration T_{eq} defined in Section 3.1. *Second row:* 2–15 Hz energy of each event, as a function of T_{eq}; a population radiating a constant energy would be flat in this plane and one radiating a constant power would rise by 10 dB per decade, so that the observed rise of about 5 dB per decade implies an instantaneous power decreasing with duration. The median band power of the background windows is quoted in each panel title as a reference level. *Third row:* hourly distribution of the detections. *Fourth row:* absolute band power of the events (coloured) and of the background windows (grey), with the hourly median of the background; the comparison shows that the hourly patterns of the third row are partly a modulation of the detection threshold and not of the sources. *Fifth row:* detection rate as a function of the day of the week, normalized to the hours actually analyzed for each weekday; the dashed line is the Monday–Friday mean.

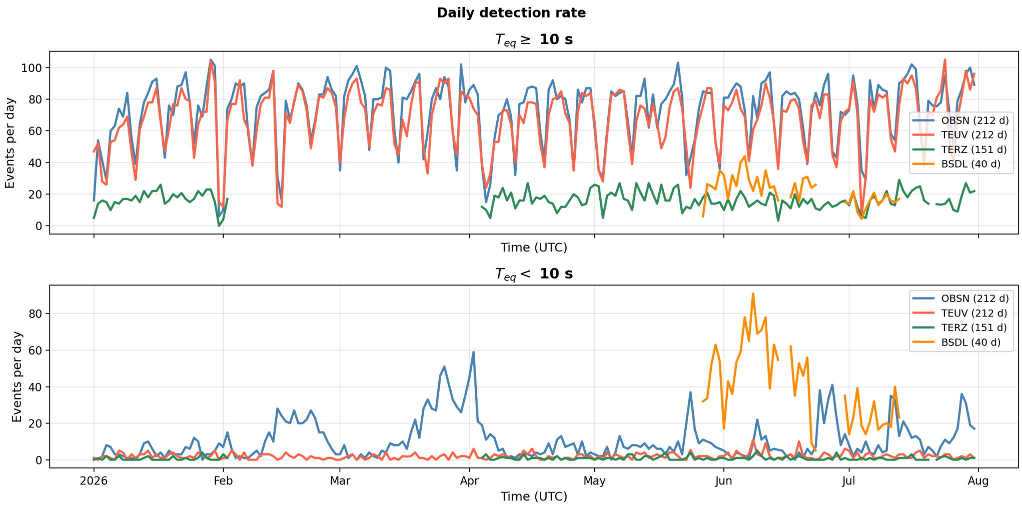

Figure 11: Daily detection rate at the four stations, split at $T_{\rm eq} = 10\,$s. *Top:* long triggers, which are the subject of Section 5.4, showing a stable weekly cycle at the stations closest to the train line. *Bottom:* short triggers, discussed in Section 5.5, which occur in isolated episodes, concentrated in time and not shared between stations.

5.4 Coincidence

The aim of this Section is not to label individual events. We try to look for structure in the catalog, using the coincidence between stations as an ordering criterion, and to describe the populations that emerge from it. BSDL is not used in this Section since the simultaneous coverage with it would restrict the comparison to a small fraction of the period.

Figure 11 shows the daily detection rate at the four stations, split at $T_{\rm eq} = 10\,$s. The two panels behave in completely different ways. The long triggers, which are the subject of this Section, follow a stable weekly cycle at OBSN and TEUV over the whole period, while the short ones appear in isolated episodes, concentrated in time and not shared between stations; they are discussed separately in Section 5.5 and are excluded from everything that follows.

Coincidence is established between the peaks of the z-score, not between the trigger onsets. The onset depends on where the envelope crosses the threshold and therefore on the signal-to-noise ratio while the peak is the closest-approach proxy and is stable against it. Matching is one-to-one within a window of $|\Delta t| \leq 100$ s. Peak times inherit the spectrogram grid of the detector, so the measured delays are quantised at 10 s. The delays discussed below are therefore transit delays and not travel times: the dominant source is a moving one, each station triggers when the convoy passes its own closest-approach point, and the inter-station delay is the along-track separation of those points divided by the speed of the convoy. Its sign reverses with the direction of travel, and no array location can be derived from it.

Because the trigger rates are high, chance associations are not negligible and are quoted throughout. For a search window $\pm W$ over an overlap of T seconds, the expected number of accidental pairs is $N_{\rm acc} \simeq N_a N_b\, 2W/T$; for the TERZ–OBSN pair at $W = 100$ s over the 151 valid days this gives ~ 500 accidental pairs against ~ 1900 matched. Since the accidental contribution is uniform in delay, it is spread over the 21 delay bins of the search window, i.e. ~ 25 events per 10 s bin, which is the flat level observed in the tails of Figure 14; it can therefore be subtracted as a constant rather than modelled, and it is negligible under the transit peaks.

OBSN is the station closest to the line and the one with the highest signal-to-noise ratio, and it is the only one in which the populations can be separated without using the coincidence at all. The left panel of Figure 12 shows the distribution of the event energy in the 2–15 Hz for the events with $T_{\rm eq} > 10$s, in which three groups can be identified and separated by two cuts; the central and right

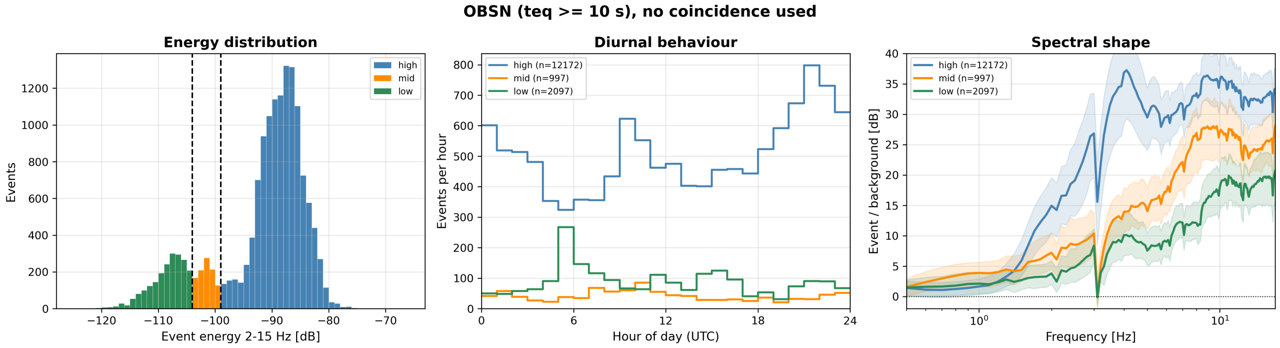

Figure 12: Classification of the events with $T_{\text{eq}} > 10\,\text{s}$ detected at OBSN, based on the event energy computed between 2 and 15 Hz; no coincidence information is used. *Left:* energy distribution and the two cuts that split the three observed peaks. *Centre:* diurnal distribution of the three classes. *Right:* spectral shape, i.e. the ratio of the event PSD over the T_{eq} window to the background PSD of the corresponding chunk, with the median and the interquartile range of each class. The rise above 15 Hz is a systematic of the different Welch segment lengths and not signal.

panels show the diurnal distribution and the spectral shape of the three classes. The high-energy class, which dominates the catalog, has a marked peak at $\sim$ 4 Hz and a nearly flat diurnal distribution, and is the class most plausibly associated with the railway passages. The mid class shows an excess during working hours and a spectral shape that keeps rising with frequency, compatible with local road traffic. The low-energy class is concentrated around 06 UTC which suggests a fixed installation, such as pumping or industrial machinery. None of these associations is established: the classes are defined by the data, and their interpretation remains tentative in the absence of an independent trigger.

At TEUV the events are fewer and weaker, and the energy distribution does not separate into classes; the coincidence with OBSN is used instead. The left panel of Figure 13 shows the distribution of the delay between the peak at TEUV and the peak at OBSN. It is clearly bimodal, with two sharp maxima at ± 40 s, which is the signature of a moving source travelling in the two directions along the line. With a separation of $\approx$ 1.1 km between the two closest-approach points, this corresponds to an average speed of $\approx$ 28 m/s, i.e. about 100 km/h, consistent with the line speed. A third, narrower peak at zero delay contains about 250 events; these are not transits, since a transit cannot produce a null delay between two points 1.1 km apart, and part of them are local earthquakes, quarry blasts and other regional activity. The central and right panels show that the coincident and the isolated populations differ both in their diurnal distribution and in their spectral shape, the isolated events being systematically weaker and lacking the 3–5 Hz structure of the coincident ones.

TERZ is used as the key for the classification of Figure 14, because it is the rarest station. A TERZ trigger is classified as *coincident* if at least one of the two anchors, OBSN or TEUV, has a peak within ± 100 s, and as *isolated* otherwise. The left panel shows the delay distributions with respect to the two anchors, which differ in shape because of the geometry: the perpendicular foot of TERZ is close to OBSN, so the delays to OBSN cluster near zero, while those to TEUV retain the bimodal transit structure. For a single transit the two delays measured against the same reference carry the same sign, and opposite signs identify accidental pairs. The isolated events at TERZ are concentrated in the early morning, which is where the relative threshold is lowest, and their spectral shape differs from that of the coincident ones without separating cleanly from it.

The earthquake class is defined against a catalog built by querying the KNMI and EMSC FDSN event service available for the period, without a magnitude floor, since quarry blasts are frequently published without magnitude. Within 120 km of the site this yields 72 unique events, of which 68 earthquakes, 3 quarry blasts and one sonic boom, with 12 events within 30 km in the magnitude range 0.2–3.0; 21 TERZ triggers match one of them. As anticipated in Appendix B, distant teleseisms do not enter the statistic, so this contamination is entirely local.

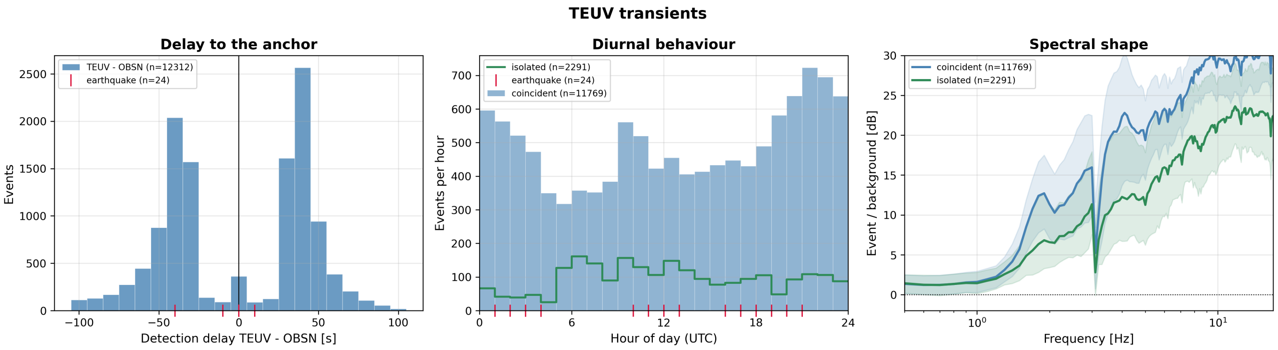

Figure 13: Transients at TEUV, classified by coincidence with OBSN. *Left:* distribution of the delay between the peak of the detection statistic at TEUV and at OBSN; the two maxima at ± 40 s correspond to the two directions of travel along the line and give an average speed of ≈ 28 m/s over a separation of ≈ 1.1 km. Red ticks mark the triggers associated with the earthquake catalog. *Centre:* diurnal distribution of the coincident, isolated and earthquake classes. *Right:* spectral shape of the coincident and isolated classes, defined as in Figure 12. Delays are quantised at 10 s by the spectrogram grid of the detector.

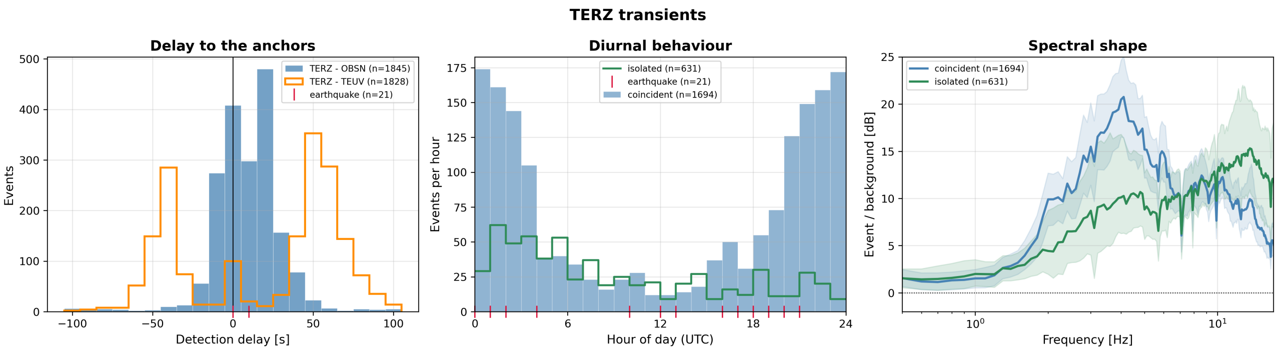

Figure 14: Transients at TERZ, classified by coincidence with the two anchors OBSN and TEUV. *Left:* delay distributions with respect to each anchor; the two differ in shape because the perpendicular of TERZ lies close to OBSN, so that the delays to OBSN cluster near zero while those to TEUV retain the bimodal transit structure. *Centre:* diurnal distribution of the coincident, isolated and earthquake classes. *Right:* spectral shape of the coincident and isolated classes.

5.5 Short transients

The triggers with $T_{\rm eq} < 10$ s at OBSN and BSDL form a population with properties opposite to those discussed so far, and are treated separately. They appear in isolated episodes showing no diurnal or weekly modulation as visible in the bottom panel of Figure 11. Remarkably, they also have no coincident trigger at the co-located surface sensors.

On the raw counts they are single impulses of 0.1–0.5 s (showing the limits of the $T_{\rm eq}$ definition for the shortest transients), reaching hundreds of times the local noise level, with no scattering tail. The absence of a tail, together with the very short rise time, suggests that a substantial fraction of their energy lies above 15 Hz, so that the durations reported here are set by the analysis band. A three-component test at BSDL shows them on all three components, with a median vertical signal-to-noise ratio of 36 dB. The comparison between the horizontal and the vertical components of the typical events at OBSN is more informative: the horizontal components are affected considerably more than the vertical one, and while the vertical component shows only a short transient, the horizontal components creep slowly back to their original level. This is the signature of a tilt of the sensor, subsequently compensated by the instrument, and therefore of a minuscule physical movement of the sensor rather than of a propagating seismic signal.

No conclusion is drawn on the nature of these triggers. Their properties are compatible with a local mechanical origin at the borehole itself, whether of the installation or of the instrument. A dedicated analysis is needed to establish whether they are instrumental glitches; until then they have been excluded from the catalog analysis of Sections 5.3 and 5.4.

6 Conclusion

We have presented the seismic characterization of the EMR candidate site based on the borehole network recently installed in the Terziet area, covering the first seven months of 2026 at four underground stations together with their co-located surface sensors. We also introduce `SiteChar`, a new Python-framework, which provides a common processing pipeline that allows to separate the stationary background from the transient contributions.

The results have to be read in the light of how the network was deployed. Most of these boreholes were deliberately positioned next to railway infrastructure and only BSDL lies close to a possible corner point, so what the network measures is how anthropogenic noise is generated and attenuated in this geology, and not the conditions achievable at a corner point.

The central methodological result is the separation between the stationary background and the transient component, made necessary by the fact that the field is non-stationary on several timescales at once. Once the fast non-stationarities are excluded, the four boreholes, drilled in different geological conditions and at distances from the railway ranging from tens of metres to several kilometres, describe essentially the same stationary field. The slower non-stationarities survive in the background spectra themselves, which retain a diurnal cycle of 5–8 dB above 1 Hz and the seasonal modulation of the microseism.

The transient population is dominated by railway traffic and is detected at all four stations, including TERZ and BSDL, more than two kilometres from the line and at 250 m depth. The coincidence between stations resolves the transit of the source along the line, giving an average speed consistent with the line speed, and separates the catalog into classes that differ in energy, in diurnal distribution and in spectral shape. During a passage the borehole and the surface sensor of the same station remain coherent above the frequency at which the ambient fields decorrelate, so that a surface sensor carries usable information on the disturbance seen at depth. At the stations far from the line the passage stays above the borehole noise floor while falling below the surface one, which quantifies event by event the gain in detectability provided by the depth.

These transients are not a marginal correction to the ambient field: they exceed the local background by tens of dB in the band where the detector is most closely coupled to its environment, and they occur a few times per hour at the stations close to the line. Current mitigation schemes are designed against a stationary field, and this is precisely where a data-driven approach, such as the neural-network subtraction being developed for the EMR site [10], has an advantage over a fixed linear filter, provided that the transient population is described realistically. Supplying that description, together with the background levels on which the propagation and NN models are built, is the contribution of this work to the integrated modelling chain currently developed for the EMR candidate site.

Acknowledgements

The authors thank all the members of the EMR noise group for the many discussions on the results presented in this paper.

Claude (Opus5) was used for code refactoring and script formatting. The final code and analysis were thoroughly tested and verified by the authors, who accept full responsibility for the software and results presented.

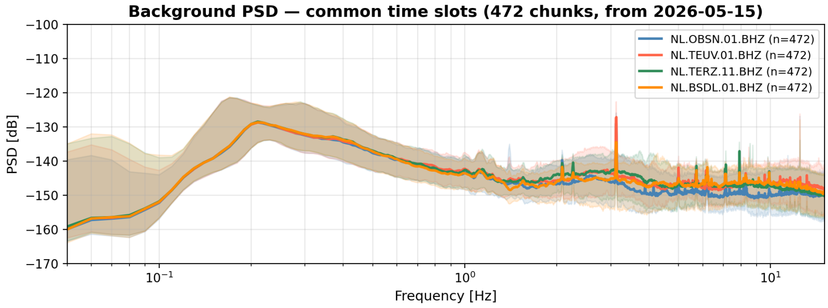

Figure 15: PSD on common chuncks between TERZ, TEUV and OBSN confirming that the microseism is the same when considering the same time periods.

A Microseism

The secondary microseismic peak at ~ 0.2 Hz dominates the spectra of all four stations below ~ 0.5 Hz, with median levels between -124 and -117 dB (Figure 5). The spread of a few dB between stations seen in that figure is not a site property but a consequence of the different temporal coverage of the four datasets, since the microseismic amplitude is modulated by the seasonal cycle of ocean-wave activity. Restricting the comparison to the two-hour chunks that are simultaneously available at OBSN, TEUV and TERZ (1095 chunks) removes the effect. Figure **??** shows that the microseismic peaks then coincide to within a fraction of a dB, both in level and in the width of the percentile band. At these frequencies the field is therefore regionally coherent and identical across the EMR area, as expected.

The origin of the modulation is confirmed by the comparison with the ocean forcing. Figure 16 shows the daily median band power in 0.1–0.3 Hz, computed on the background windows only, together with the significant wave height (SWH) area-averaged over the North Atlantic (40–65°N, 40°W–5°E) from the ERA5 reanalysis. The two series track each other closely over the whole observation period, including the individual storm episodes of January–March and the decay towards May–June, with a Pearson correlation coefficient $r = 0.89$ at both OBSN and TEUV. This is the behaviour expected from the double-frequency generation mechanism, in which the seismic power scales with the interaction of opposing wave trains in the source region.

B Earthquakes

Earthquakes appear in the time evolution of the background spectra (Figure 4) as coincident horizontal stripes, i.e. as short-lived excursions that are broadband in frequency and simultaneous at all stations. They are a natural population of transients, distinct from the anthropogenic one that is the subject of Section 5, and it is useful to establish how they enter the detection statistic.

Candidate events are identified by cross-matching the times of the stripes with a global earthquake catalog, and the automated detection follows the same time-frequency z-score methodology developed in Section 3.1, applied to the same 2–15 Hz band. Theoretical body-wave travel times t_P and t_S are computed with the `iasp91` velocity model through `obspy` and used to verify the association. Figure 17 shows a representative case, the M_w 7.4 Miyako (Japan) earthquake of 2026-04-20 recorded at TERZ: the instrument-corrected acceleration waveform shows the arrivals at the predicted times, and the wave train is clearly visible in the low-frequency part of the spectrogram.

The response of the detector to such events is, however, modest. The energy of a distant teleseism reaching the site is concentrated below ~ 1 Hz, whereas the statistic is evaluated as a median over 2–15 Hz and responds only when the majority of the bins in that band rise together. Earthquakes of this class therefore produce no excursion of $z(t)$. The catalog discussed in Section 5 is not appreciably contaminated by strong world-wide earthquakes but it is contaminated by the local and micro

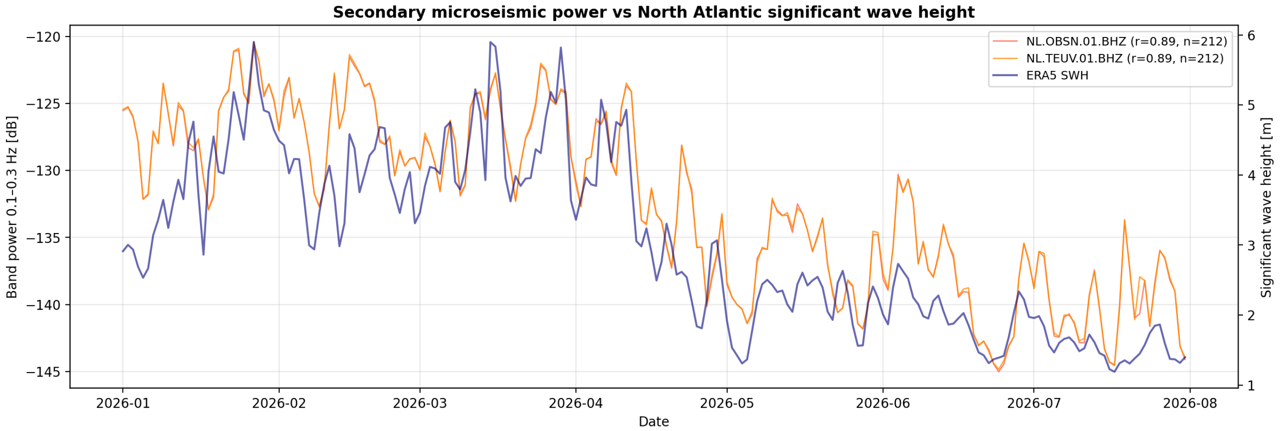

Figure 16: Daily median microseismic band power (0.1–0.3 Hz, background windows) at OBSN and TEUV compared with the area-averaged significant wave height (SWH) over the North Atlantic (40–65°N, 40°W–5°E) from ERA5 reanalysis. Both seismic stations track the ocean wave forcing closely, with Pearson correlation coefficients reported in the legend. The strong positive correlation confirms that the secondary microseismic peak observed at the ET candidate site is driven by North Atlantic storm activity, consistent with the double-frequency generation mechanism. The dual y-axis shows seismic power in dB (left) and SWH in metres (right).

earthquakes of the region.

C Z-score detection and limits of T_{eq} definition

- For low SNR the Teq is spread. It is a good measure only for high SNR
    - for very short events it is a mess

References

[1] M Punturo et al. "The Einstein Telescope: a third-generation gravitational wave observatory". In: *Classical and Quantum Gravity* 27.19 (2010), p. 194002. DOI: 10.1088/0264-9381/27/19/194002. URL: https://doi.org/10.1088/0264-9381/27/19/194002.

[2] S Hild et al. "Sensitivity studies for third-generation gravitational wave observatories". In: *Classical and Quantum Gravity* 28.9 (2011), p. 094013. DOI: 10.1088/0264-9381/28/9/094013. URL: https://doi.org/10.1088/0264-9381/28/9/094013.

[3] A. Abac et al. "The Science of the Einstein Telescope". In: *JCAP* 03 (2026), p. 081. DOI: 10.1088/1475-7516/2026/03/081. arXiv: 2503.12263 [gr-qc].

[4] F. Amann et al. "Site-selection criteria for the Einstein Telescope". In: *Review of Scientific Instruments* 91.9 (Sept. 2020), p. 094504. ISSN: 0034-6748. DOI: 10.1063/5.0018414. eprint: https://pubs.aip.org/aip/rsi/article-pdf/doi/10.1063/5.0018414/14800145/094504_1_online.pdf. URL: https://doi.org/10.1063/5.0018414.

[5] J. Harms. "Terrestrial gravity fluctuations". In: *Living Reviews in Relativity* 22.1 (2019), p. 6. DOI: 10.1007/s41114-019-0022-2.

[6] M. W. Coughlin et al. "Implications of Dedicated Seismometer Measurements on Newtonian-Noise Cancellation for Advanced LIGO". In: *Phys. Rev. Lett.* 121.22 (2018), p. 221104. DOI: 10.1103/PhysRevLett.121.221104.

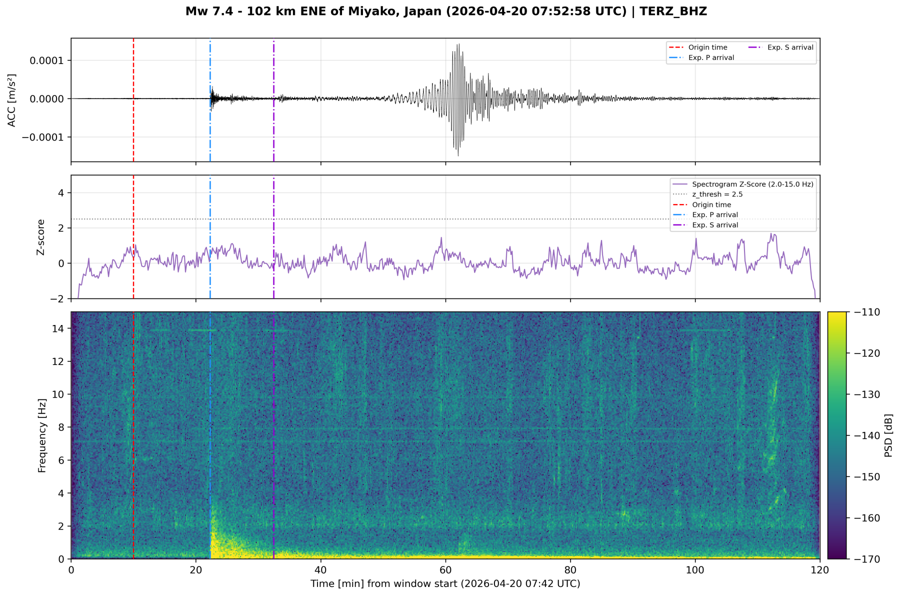

Figure 17: Seismic signal analysis of the M_w 7.4 Miyako, Japan earthquake recorded at station TERZ. *Top panel:* Instrument-corrected acceleration waveform (m/s^2). *Middle panel:* Spectrogram Z-score time profile computed in the $[2.0, 15.0]$ Hz frequency band; the horizontal dotted line marks the detection threshold ($z_{\text{thresh}} = 2.5$). *Bottom panel:* Power Spectral Density (PSD) spectrogram in dB. In all panels, the red dashed line denotes the event Origin Time (2026-04-20 07:52:58 UTC), while the blue and purple dash-dotted lines indicate the theoretical P-wave and S-wave arrival times computed via the `iasp91` model in `obspy`.

[7] F. Badaracco et al. "Optimization of seismometer arrays for the cancellation of Newtonian noise from seismic body waves". In: *Class. Quantum Grav.* 36.14 (2019), p. 145006. DOI: 10.1088/1361-6382/ab28c1. arXiv: 1903.07936 [astro-ph.IM].

[8] P. Schillings et al. "Optimization and robustness of cost-efficient seismic arrays for Newtonian noise cancellation at the Einstein Telescope". In: (June 2026). arXiv: 2606.21110 [astro-ph.IM].

[9] V. van Beveren et al. "A study of deep neural networks for Newtonian noise subtraction at Terziet in Limburg—the Euregio Meuse-Rhine candidate site for Einstein Telescope". In: *Classical and Quantum Gravity* 40.20 (2023), p. 205008. DOI: 10.1088/1361-6382/acf3c8. URL: https://doi.org/10.1088/1361-6382/acf3c8.

[10] J. Kelleter et al. "NNNN: Neural Networks for Newtonian Noise Mitigation at the Einstein Telescope". In: (June 2026). arXiv: 2606.19907 [astro-ph.IM].

[11] M. Bader et al. "Newtonian-noise characterization at Terziet in Limburg—the Euregio Meuse–Rhine candidate site for Einstein Telescope". In: *Classical and Quantum Gravity* 39.2 (2022), p. 025009. DOI: 10.1088/1361-6382/ac1be4. URL: https://doi.org/10.1088/1361-6382/ac1be4.

[12] S. Koley et al. "Surface and underground seismic characterization at Terziet in Limburg—the Euregio Meuse–Rhine candidate site for Einstein Telescope". In: *Classical and Quantum Gravity* 39.2 (2022), p. 025008. DOI: 10.1088/1361-6382/ac2b08. URL: https://doi.org/10.1088/1361-6382/ac2b08.

Figure 18: Detection statistic $z(t)$ over the same chunk of Figure 6, for the borehole sensors (**??**) and for the co-located surface sensors (**??**). The dashed horizontal line is the detection threshold $z_{\text{thresh}} = 2.5$; the orange band is the trigger analyzed and the dashed orange lines delimit its T_{eq} window; the red bands are the other triggers of the same sensor, taken from the catalog for the borehole and detected locally for the surface; the green band is the background window actually used, i.e. the longest stretch in which neither sensor of the station has a trigger, with a guard of 60 s. At TERZ and BSDL the surface statistic does not cross the threshold inside the T_{eq} window of the borehole, and the event is treated there as an upper limit.